

PROCEEDINGS OF SPIE

[SPIDigitalLibrary.org/conference-proceedings-of-spie](https://spiedigitallibrary.org/conference-proceedings-of-spie)

Sparse view Compton scatter tomography with energy resolved data: experimental and simulation results

Abdulla Desmal
Brian H. Tracey
Hamideh Rezaee
Eric L. Miller
Jeffrey R. Schubert
Jeff Denker
Aaron Couture

Sparse view Compton scatter tomography with energy resolved data: experimental and simulation results

Abdulla Desmal^a, Brian H. Tracey^a, Hamideh Rezaee^a, Eric L. Miller^a, Jeffrey R. Schubert^b,
Jeff Denker^b, and Aaron Couture^b

^aTufts University, Medford, Massachusetts, USA

^bAmerican Science and Engineering, Inc., Billerica, Massachusetts, USA

ABSTRACT

X-ray inspection systems play a critical role in many non-destructive testing and security applications, with systems typically measuring attenuation during transmission along straight-line paths connecting sources and detectors. Computed tomography (CT) systems can provide higher-quality images than single- or dual-view systems, but the need to measure many projections through the scene increases system complexity and cost. We seek to maximize the image quality of sparse-view (few-view) systems by combining attenuation data with measurements of Compton-scattered photons, that deflect after scattering and arrive at detectors via broken ray paths that provide additional sampling of the scene. The work below presents experimental validation of a single-scatter forward model for Compton-scatter data measured with energy-resolving detectors, and demonstrates a reconstruction algorithm that combines both attenuation and scatter measurements. The results suggest that including Compton-scattered data in the reconstruction process can improve image quality for few-view systems.

Keywords: Compton scatter, broken-ray, tomography, baggage screening, X-ray

1. INTRODUCTION

X-ray inspection plays an important role in medical,¹ industrial² and airport security^{3,4} applications. While single-energy systems are most common, much recent development in X-ray inspection has focused on improving material identification (for example estimating the density and photoelectric coefficient of objects) by use of dual- and multi-energy CT acquisition systems.^{5,6} Specifically, the results in^{7,8} suggest that energy resolving systems perform more robustly for material characterization. Energy-resolving detectors have also been shown to improve material identification in scenes including highly attenuating objects,⁹ an important advantage in luggage screening applications where metal objects are frequently encountered.

CT systems used in medical imaging are generally able to collect data projections at a large number of angles fully encircling the object. In contrast, in many security applications including luggage screening and kVp spectral CT,¹⁰ access to the object from different views are limited while material characterization remains quite critical. There have been a variety of investigations into limited-view tomography methods, several of which exploit energy-resolved measurements and enforce similarity across energy channels.¹⁰⁻¹² However, the limited-view CT problems remains quite challenging.

Our hypothesis is that image quality can be improved in limited-view tomography by processing not only straight-line attenuation projections through the object, but also broken-ray data whereby photons travel from the source to a scattering object, deflect via Compton scattering to a new angle (with corresponding energy shift), and then are measured at a detector. Including these broken-ray paths in the inversion process dramatically increases the number of geometric ray paths through the investigation domain, and thus holds the potential to reduce image artifacts. However, processing this scattered data (typically regarded as noise in CT) brings several challenges, notably the low number of counts associated with these raypaths and the computational burden of modeling the additional paths (the forward model for Compton scatter tomography models attenuation from the

Further author information: (Send correspondence to B.H.T.)

B.H.T.: E-mail: btracey@eecs.tufts.edu, Telephone: 1 617 627 6424

E.L.M.: E-mail: elmiller@eecs.tufts.edu, Telephone: 1 617 627 3220

source to the scattering point, the scattering process itself, and attenuation of the scattered photon as it travels to the detector).

Compton scatter tomography has been explored previously and has been shown to have advantages over conventional CT systems in nondestructive evaluation applications¹³ and materials characterization.¹⁴ More specifically, Compton scattering is sensitive to structural and density variation within the object¹⁵ by providing a strong contrast mechanism comparing to total attenuation.¹⁶ Analytic Compton scattering tomography reconstruction methods are available, but are limited to specific data acquisition geometries.^{17,18} Numerical reconstruction algorithms, such as the one discussed in this paper, are applicable to more general geometries. Unlike the work presented here, many previous publications either assume that an X-ray attenuation map is known a priori from a traditional CT scan (resulting in a linear mapping from density to observations),¹⁶ or do not fully model the energy dependence of the attenuation.^{19,20} Our forward model is more closely related to that in,²¹ although that work includes fluorescence effects which are not important in our application and also seeks to recover a fluorescence attenuation map.

The remainder of this paper is organized as follows. In Section II, we describe the system geometries of interest and introduce the models we use for both energy resolved Compton scatter data (see⁹ for a more complete description of our model for attenuation data). We also introduce an reconstruction algorithm that combines both attenuation and scatter measurements. In Section III we describe an experimental testbed and present comparisons of experimental data and forward model predictions, showing good agreement in both energy-integrated and energy-resolved measurements. Because data from the initial experimental exhibited several notably artifacts (not discussed here in detail), we present simulation results showing the advantage of reconstructions that use both scattered data and attenuation (transmission) measurements. Finally, we conclude and discuss future work.

2. FORMULATION

In this section we first describe our forward model for Compton-scattered data in detail (transmission data are processed using the forward model discussed in⁹). We then outline the reconstruction algorithm used to combine both types of data.

2.1 Forward model for Compton scattering

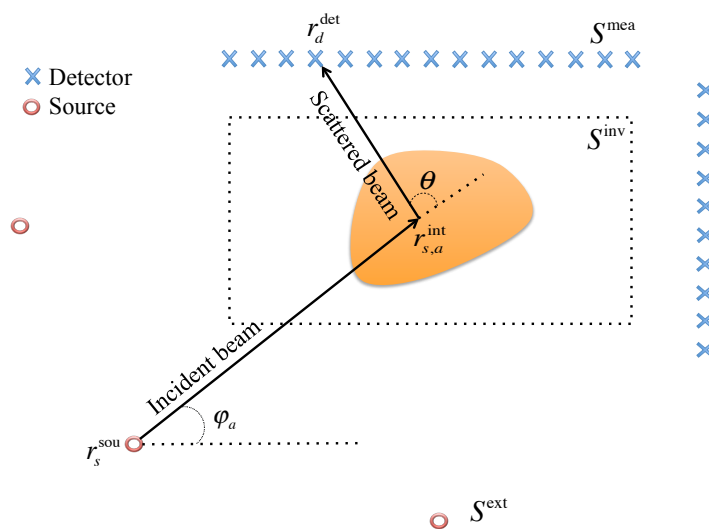


Figure 1. Problem configuration.

Figure 1 illustrates a two-dimensional cross section of the problem configuration, where the slice plot is over the $x - y$ plane while the z -axis is assumed to be invariant. This scenario models a pencil-beam X-ray source

scanning across the investigation domain. Three domains are shown in the figure, labeled as S^{inv} , S^{exc} and S^{mea} . S^{inv} is the investigation domain where the object(s) being imaged are located, S^{exc} is the excitation domain, and finally, S^{mea} is the measurement domain where the detectors are located. $r_s^{\text{sou}} \in S^{\text{exc}}$ and $r_d^{\text{det}} \in S^{\text{det}}$ are position vectors that points to source and detector locations, respectively. Here $s = 1, 2, \dots, N^{\text{sou}}$ denotes the source, with N^{sou} being the number of source locations. Similarly $d = 1, 2, \dots, N^{\text{det}}$ denotes the number of detectors, with N^{det} being the number of detector locations. The source at location r_s^{sou} illuminates the investigation domain at multiple incident beam angles ϕ_a , $a = 1, 2, \dots, N^{\text{ang}}$, where N^{ang} is the number of angles per source location, (see Figure 1). $r_{s,a}^{\text{int}} \in S^{\text{inv}}$ is position vector that points to an interaction point inside the investigation domain, that lies within an incident beam due to source s and angle a . In Figure 1, the incident X-ray beam will emit from source location r_s^{sou} at angle ϕ_a . While crossing the investigation domain it will interact with material inside, which will cause non-coherent Compton scattering, on position $r_{s,a}^{\text{int}}$. The number of photons collected at detector r_d^{det} , due to interaction point $r_{s,a}^{\text{int}}$ for incident energy E^{inc} is given by:

$$g(r_s^{\text{sou}}, r_{s,a}^{\text{int}}, r_d^{\text{det}}, E^{\text{inc}}) = \frac{I(E^{\text{inc}}) H(r_s^{\text{sou}}, r_{s,a}^{\text{int}}, E^{\text{inc}}) S(r_s^{\text{sou}}, r_{s,a}^{\text{int}}, r_d^{\text{det}}, E^{\text{inc}}) H(r_{s,a}^{\text{int}}, r_d^{\text{det}}, E^{\text{sca}}) \rho(r_{s,a}^{\text{int}}) \Omega(r_{s,a}^{\text{int}}, r_d^{\text{det}})}{I(E^{\text{inc}}) H(r_s^{\text{sou}}, r_{s,a}^{\text{int}}, E^{\text{inc}}) S(r_s^{\text{sou}}, r_{s,a}^{\text{int}}, r_d^{\text{det}}, E^{\text{inc}}) H(r_{s,a}^{\text{int}}, r_d^{\text{det}}, E^{\text{sca}}) \rho(r_{s,a}^{\text{int}}) \Omega(r_{s,a}^{\text{int}}, r_d^{\text{det}})} \quad (1)$$

where $I(E^{\text{inc}})$ is the number of photons emitted by the source at energy E^{inc} . $H(r_s^{\text{sou}}, r_{s,a}^{\text{int}}, E^{\text{inc}})$ computes the incident beam attenuation that occurs while the incident photons travel from source location r_s^{sou} to interaction point $r_{s,a}^{\text{int}}$. Similarly, $H(r_{s,a}^{\text{int}}, r_d^{\text{det}}, E^{\text{sca}})$ computes scattered beam attenuation while the scattered photons travel from interaction point $r_{s,a}^{\text{int}}$ to detector location r_d^{det} . Notice that Compton scattering is non-coherent, hence the attenuation after scattering $H(r_{s,a}^{\text{int}}, r_d^{\text{det}}, E^{\text{sca}})$ will depend on the photon scattering energy E^{sca} which is described in Eq. 4. The function $S(r_s^{\text{sou}}, r_{s,a}^{\text{int}}, r_d^{\text{det}}, E^{\text{inc}})$ computes the fraction of photons scattered toward detector r_d^{det} at interaction point $r_{s,a}^{\text{int}}$ due to source location r_s^{sou} . $\rho(r_{s,a}^{\text{int}})$ is the material density evaluated at interaction point $r_{s,a}^{\text{int}}$. Finally, $\Omega(r_{s,a}^{\text{int}}, r_d^{\text{det}})$ is the solid angle function of a rectangular detector at r_d^{det} viewed from interaction point $r_{s,a}^{\text{int}}$. In the following, computation of Eq. 1 is further described. The attenuation functions are computed as

$$H(r^{\text{sta}}, r^{\text{end}}, E) = \exp\left(-\int_{l(r^{\text{sta}}, r^{\text{end}})} \mu(r', E) dl'\right) \quad (2)$$

where r^{sta} is the start of the attenuated beam, r^{end} is the end of the attenuated beam and E is the photon energy. The integral inside the exponent function is a line integral that runs from r^{sta} to r^{end} . The integrand $\mu(r, E)$ is the attenuation coefficient function, given by

$$\mu(r, E) = N_A \frac{Z(r)}{A(r)} \rho(r) f_{KN}(E) + p(r) f_p(E) \quad (3)$$

where N_A is the Avogadro number and $Z(r)$ and $A(r)$ are the atomic and mass numbers, respectively. $\rho(r)$ and $p(r)$ are the material density and photoelectric coefficients, while $f_p(E) = (E_0/E)^3$ is the photoelectric energy factor with E_0 as the referenced energy. The energy factor of the Compton scattering is given by the Klein-Nishina cross section

$$f_{KN}(E) = \frac{1 + \alpha}{\alpha^2} \left[\frac{2(1 + \alpha)}{(1 + 2\alpha)} - \frac{1}{\alpha} \ln(1 + 2\alpha) \right] + \frac{1}{2\alpha} \ln(1 + 2\alpha) - \frac{1 + 3\alpha}{(1 + 2\alpha)^2}$$

where $\alpha = E^{\text{inc}}/(m_e c^2)$, where m_e and c are the electron mass and speed of light, respectively. In Eq. 1, the scattered photon energy E^{sca} is

$$E^{\text{sca}} = \frac{E^{\text{inc}}}{1 + \alpha(1 - \cos(\theta(r_s^{\text{sou}}, r_{s,a}^{\text{int}}, r_d^{\text{det}})))} \quad (4)$$

where the angle $\theta(r_s^{\text{sou}}, r_{s,a}^{\text{int}}, r_d^{\text{det}})$, as shown in Figure 1, is computed as follows

$$\theta(r_s^{\text{sou}}, r_{s,a}^{\text{int}}, r_d^{\text{det}}) = \cos^{-1} \left(\frac{\langle r_{s,a}^{\text{int}} - r_s^{\text{sou}}, r_d^{\text{det}} - r_{s,a}^{\text{int}} \rangle}{|r_{s,a}^{\text{int}} - r_s^{\text{sou}}| |r_d^{\text{det}} - r_{s,a}^{\text{int}}|} \right). \quad (5)$$

Referring back to Eq. 1, the scattering factor $S(r_s^{\text{sou}}, r_{s,a}^{\text{int}}, r_d^{\text{det}}, E^{\text{inc}})$ is computed as follows:

$$S(r_s^{\text{sou}}, r_{s,a}^{\text{int}}, r_d^{\text{det}}, E^{\text{inc}}) = N_A \frac{Z(r_{s,a}^{\text{int}})}{A(r_{s,a}^{\text{int}})} \frac{r_e^2}{2[1 + \alpha(1 - \cos\theta)^2]} \left[(1 + \cos^2\theta) + \frac{\alpha^2(1 - \cos\theta)^2}{1 + \alpha(1 - \cos\theta)} \right]$$

where r_e is the electron radius and θ is given by Eq. 5.

Note that Eq. 1 computes the scattered photons over a particular interaction point due to a single incident energy. The total number of photons scattered from all the interaction points lying across the incident beam and scattered toward the detector location r_d^{det} at a given energy E is computed as

$$g_{s,a,d}^{\text{tot}}(E) = \int_{E^{\text{inc,low}}}^{E^{\text{inc,high}}} \int_{l(r_s^{\text{sou}}, r^{\text{end}})} g(r_s^{\text{sou}}, r_{s,a}^{\text{int}}, r_d^{\text{det}}, E^{\text{inc}}) \delta(E - E^{\text{sca}}) dl^{\text{int}} dE^{\text{inc}} \quad (6)$$

where $l(r_s^{\text{sou}}, r^{\text{end}})$ is the path traversed by the a -th angle beam, and r^{end} is the end point where the beam leaves the system. Let $\bar{g}_{s,a,d}$ be a vector that store samples of $g_{s,a,d}^{\text{tot}}(E)$ for different energies E_i , $i = 1, 2, \dots, N^{\text{enr}}$, where N^{enr} is the number of detector energy bins:

$$\bar{g}_{s,a,d} = \begin{bmatrix} g_{s,a,d}^{\text{tot}}(E_1) \\ g_{s,a,d}^{\text{tot}}(E_2) \\ \vdots \\ g_{s,a,d}^{\text{tot}}(E_{N^{\text{enr}}}) \end{bmatrix} \quad (7)$$

The measured data recorded by the multi-energy detectors are affected by the interaction of photons inside the detector.⁶ The detector response matrix \bar{D} accounts for this interaction. Letting \bar{m} be a vector that stores the samples produced by the multi-energy detector, we compute:

$$\bar{m}_{s,a,d} = \bar{D} \bar{g}_{s,a,d} \quad (8)$$

Assume that the investigation domain S^{inv} is discretized using equal sized pixels, with N^{cel} being the number of discretized cells. The line integrals in Eqs. 2 and 6 will be evaluated using Riemann sum of the paths discretized over the grid.²² Let $\bar{\rho}$ and \bar{p} be $N^{\text{cel}} \times 1$ vectors that store samples of $\rho(r)$ and $p(r)$ with position r evaluated at the discretized cell centers. Let \bar{m} be a vector that cascades the discretized version of $\bar{m}_{s,a,d}$ over all s,a and d , and let $f(\bar{\rho}, \bar{p})$ be the function that computes all the entries of \bar{m} , given in term of the material coefficients (density and photoelectric coefficient). $f(\bar{\rho}, \bar{p})$ computed as described by the r.h.s of Eq. 8, and Eqs. 7, 6 and 1. The output of the forward model will then be written as:

$$\bar{m} = f(\bar{\rho}, \bar{p}) \quad (9)$$

For the sake of clarity, \bar{m} denotes the calculated output of the forward model. Real data collected from the experiment will be cascaded just as explained with \bar{m} but will be referred to as vector \bar{d} .

2.2 Reconstruction algorithm

This section describes the reconstruction algorithm, which uses both transmission (Tx) and scatter data to image material properties. As the photoelectric coefficient has relatively small impact on the measurement if compared to the density, its reconstruction process is challenging.²³ The focus on this paper will illustrate density reconstruction only, while photoelectric reconstruction will be investigated in future work. The Tx data are processed using the sinogram decommission approach explained in,⁹ which is used to decompose the Tx data into photoelectric and density sinograms. With use of a transmission system matrix \bar{T} , a linear system can be built to relate the density and photoelectric coefficients to their sinograms.

$$\hat{\rho} = \arg \min_{\bar{\rho}} \left\{ 0.5\gamma^{\text{sca}} \|f(\bar{\rho}, \bar{p}) - \bar{d}\|_2^2 + 0.5\gamma^{\text{tra}} \|\bar{T}\bar{\rho} - \bar{s}^{\text{den}}\|_2^2 + \lambda^{\text{TV}} |\nabla \bar{\rho}|_1 \right\} \quad (10)$$

where γ^{sca} , γ^{tra} and λ^{TV} are optimization parameters used to weight the Compton scattering data misfit, transmission density sinogram misfit and the regularization term, respectively. The regularization term is needed to tackle the ill-posedness of the inverse optimization problem. Here total variation (TV) regularization is used which is computed as the first-norm of the density gradient, and λ^{TV} is the regularization parameter. The total variation penalty promotes or enhances the edge content of images. In Eq. 10, \bar{s}^{den} is the density sinogram. To solve the problem in Eq. 10, an estimation of the photoelectric coefficient $\bar{\rho}$, must be known. Due to the fact that $\bar{\rho}$ has small contribution to the measurement \bar{d} , it will be assumed to be zero. The optimization problem, Eq. 10, is then solved using a steepest descent algorithm

- Step 1.0 : $\bar{\rho}_0 = 0, \bar{p}_0 = 0$
 Step 2.0 : Determine $\gamma^{\text{sca}}, \gamma^{\text{tra}}, \lambda^{\text{TV}}, \beta$
 Step 3.0 : for $i = 0, 1, \dots, N^{\text{SD}}$
 Step 3.1 :
$$\bar{\rho}_{i+1} = \bar{\rho}_i - \gamma^{\text{sca}} \omega_i^{\text{sca}} \partial_{\bar{\rho}_i} f(\bar{\rho}_i, \bar{p}_0)^* (f(\bar{\rho}_i, \bar{p}_0) - \bar{d}) - \gamma^{\text{tra}} \omega^{\text{tra}} \bar{T}^* (\bar{T} \bar{\rho}_i - \bar{s}^{\text{den}}) - \lambda^{\text{TV}} \nabla \cdot \left(\frac{\nabla \bar{\rho}_i}{\sqrt{|\nabla \bar{\rho}_i|^2 + \beta}} \right)$$

 Step 3.2 : end loop

Step 1 sets the initial density and photoelectric coefficient to zero. Step 2 sets the optimization parameters, where $\beta < 1$ is a small positive real number used to remove the derivative singularity of the TV regularization term in Eq. 1. Step 3 is the main loop of the algorithm that computes the steepest descent iteration steps and is known as Landweber algorithm,²⁴⁻²⁶ where N^{SD} is the number of steepest descent iterations. Step 3.1 computes the steepest descent iteration, where $\partial_{\bar{\rho}_i} f(\bar{\rho}_i, \bar{p}_0)^*$ is the adjoint derivative operator of the nonlinear Compton scattering solver $f(\bar{\rho}_i, \bar{p}_0)$. The iteration step size of the Compton scattering model and transmission model are determined by ω_i^{sca} and ω^{tra} , which are computed as the reciprocal of the maximum singular values of $\partial_{\bar{\rho}_i} f(\bar{\rho}_i, \bar{p}_0)$ and \bar{T} , respectively. The last term in Step 3.1 is the derivative of the relaxed TV regularization $\lambda^{\text{TV}} \sqrt{|\nabla \bar{\rho}_i|^2 + \beta}$ which approaches TV regularization as $\beta \rightarrow 0$.

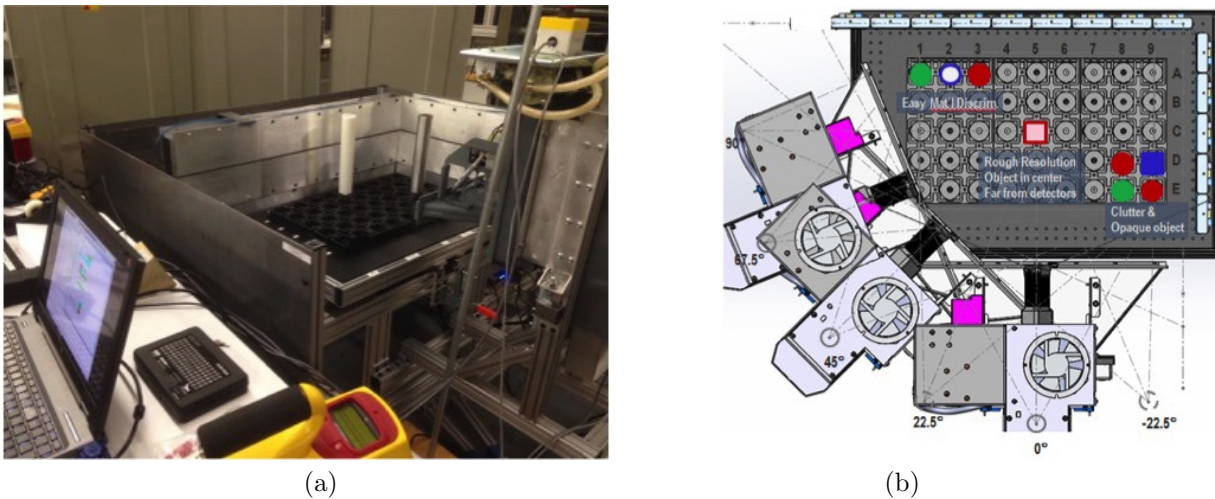


Figure 2. Experiment setup, showing (a) Picture of the testbed and (b) Layout of the experiment.

3. NUMERICAL RESULTS

In this section, experimental and simulation results are illustrated to verify the forward model and to study some simulated reconstruction results of density.

3.1 Experimental testbed

A multi-energy X-ray testbed system was constructed to experimentally measure both transmission and Compton scattering in a controlled environment using energy-discriminating detectors. This testbed, shown in Fig. 2, consists of an L-shaped detector array mounted on an optical table. The detector array consists of ME-100 photon-counting detectors (Multix, Inc., Moirans, France), arranged in 14 modules each containing 128 detectors. Five modules were arranged on one side of the L with 9 on the other (giving 1792 detectors in total, with 640 detectors distributed over $x = 41.96$ cm and $-26.53 \leq y \leq 25.6$ cm while the remaining 1152 detectors are distributed over $y = 26.75$ cm and $-53.32 \leq x \leq 40.71$ cm). A lead collimator was used to eliminate scatter from objects not in the vertical plane of the detectors. During data collection, detectors were operated at the finest energy resolution, outputting 128 evenly spaced energy channels from 20-160 keV. This represents an over-sampling, as the actual energy resolution of the ME100 is closer to 5 keV.

A roughly 60 cm x 40 cm section of the optical table was outfitted with regular 2" x 2" indentations that allow the repeatable positioning of material samples and other image targets. Both 2" square and 2" diameter circular test objects were used. The objects were interrogated using a single X-ray source (bremsstrahlung spectrum with peak energy 160 keV and average energy 62 keV) emitting a pencil beam which was swept across the detector array. This source was mounted on a pivot and could be precisely moved to interrogate the scene from different angles. In this work, we consider three source locations, namely a 0 degree source at $(x, y) = (-76.2, 0)$ cm, a 45 degree source at $(-53.88, -53.88)$ cm and a 90 degree source at $(0, -76.2)$ cm. There are total of 1792 detectors,

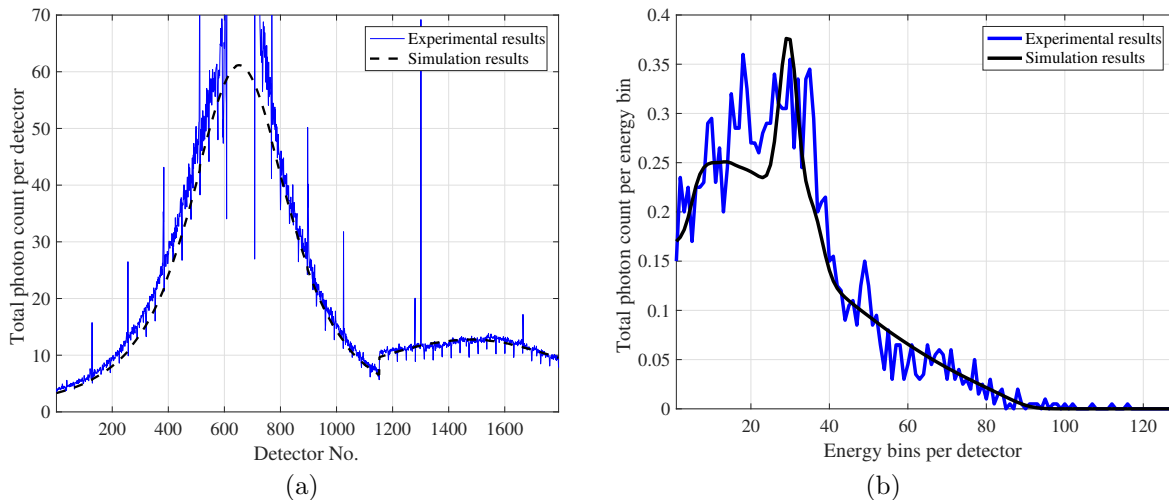


Figure 3. Forward model verification (a) Total photon counts per detector, and (b) Photon counts per energy bin at detector 1550.

3.2 Forward model verification

A Delrin (CH_2O) target of 2.54 cm radius is placed at the center of the experimental fixture. The X-ray source is located at 0 degrees while the beam angle is directed toward the object center. Figure 3(a) shows the sum of photon counts over all the energies at each detector using both experimental and simulation results. In the experimental results, the photons are collected over 0.1 msec time slots and are then averaged over 200 time slots for a total integration time of 20 sec. On the other hand, Figure 3(b), shows the number of photon counts per energy at detector number 1550, for both simulation and experiment. In Figure 3, the simulation results show an excellent match to the experimental results.

3.3 Reconstruction via simulation

In this simulation example, the investigation domain contains three targets, PVC ($\text{C}_2\text{H}_3\text{Cl}$) located at $(7.62, 7.62)$ cm, Delrin (CH_2O) located at $(0, 0)$ cm and HDPE (C_2H_4) located at $(-7.62, -7.62)$ cm. The X-ray sources are located at $(-76.2, 0)$ cm, $(-53.88, -53.88)$ cm and $(0, -76.2)$ cm. At each source location, 53 incident beam

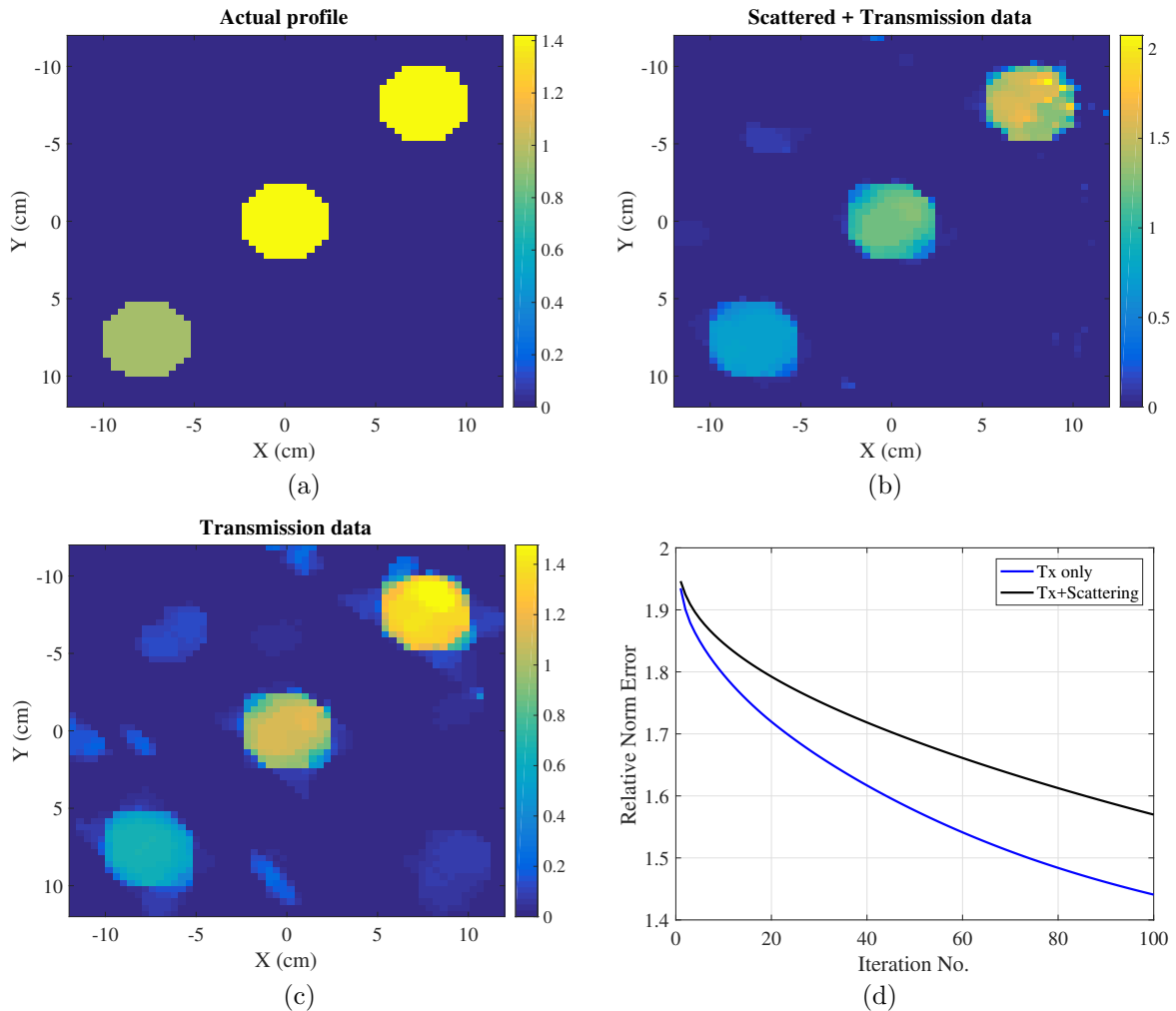


Figure 4. Simulated reconstructed result, showing (a) Actual density profile, (b) Reconstruction using both transmission and scattering data, (c) Reconstruction via transmission only, and (b) Log of relative norm error versus iteration number.

angles were used. The measurements are collected over 256 detectors. The actual profile of density is shown on Figure 4(a). To illustrate the benefit of Compton scattering data, two reconstruction tests are carried, i) using both Compton scattering data and transmission data, $\lambda^{\text{sca}} = 1$ and $\lambda^{\text{tra}} = 1$, and ii) using only transmission data, $\lambda^{\text{sca}} = 0$ and $\lambda^{\text{tra}} = 1$. Under both tests, $\lambda^{\text{TV}} = 0.1$. Figures 4(b) and 4(c) show the density profile reconstructions under both assumptions, while Figure 4(d) shows the profile relative norm error of both tests. The results clearly illustrate the benefit of contributing Compton scattering data to the inversion algorithm as the profile details noticeably improved.

4. DISCUSSION AND FUTURE WORK

The previous section demonstrated that the forward model developed in this work matches experimental data closely, and that the proposed reconstruction method is capable of incorporating scatter and transmission measurements in an inversion scheme which can produce better output than reconstructions using transmission data only. The initial testbed demonstrated some data artifacts, but the testbed has been redesigned to mitigate these artifacts. We anticipate demonstrating density reconstructions from data using measurements that will be made on the improved testbed.

The reconstruction of density, discussed in the previous sections, is relatively well-posed as compared to

reconstruction of photoelectric absorption coefficients. This is attributed to the fact that the measured data are weakly correlated with the photoelectric coefficient in Eq. 1, due to the low sensitivity of absorption on photoelectric coefficient (see Eq. 3). In the future work, in order to recover an accurate photoelectric profile image, an approach based on regularization by denoising with non-local mean filtering will be studied.^{27,28} Additionally, schemes based on multi-objective optimization can be exploited to effectively balance the data misfits of both the transmission and scattering data. We anticipate that these or related methods will lead to improved reconstruction of photoelectric absorption in the scene, leading to an improved ability to estimate material parameters.

ACKNOWLEDGMENTS

This material is based upon work supported Department of Homeland Security (DHS) Science and Technology Directorates (S&T), Homeland Security Advance Research Projects Agencies (HSARPA), Office of University Programs, under Grant Award 2013-ST-061-ED0001 and through contract #HSHQDC-15-C-B0012. The views and conclusions contained in this document are those of the authors and should not be interpreted as necessarily representing the official policies, either expressed or implied, of the U.S. Department of Homeland Security.

REFERENCES

- [1] Hiriyannaiah, H. P., “X-ray computed tomography for medical imaging,” *Signal Processing Magazine, IEEE* **14.2**, 42–59 (1997).
- [2] Hentschel, M. P., w. Harbich, K., and Lange, A., “Nondestructive evaluation of single fibre debonding in composites by x-ray refraction,” *NDT and E International* **27.5**, 275–280 (1994).
- [3] Jin, P. e. a., “A model-based 3d multi-slice helical ct reconstruction algorithm for transportation security application,” *Second International Conference on Image Formation in X-Ray Computed Tomography Salt Lake City, Utah, US* (2012).
- [4] Singh, S. and Singh, M., “Explosives detection systems (eds) for aviation security,” *Signal Processing* **83**(1), 31–55 (2003).
- [5] Shikhaliev, P. M., “Energy-resolved computed tomography: first experimental results,” *Physics in Medicine and Biology* **53**(20), 595–613 (2008).
- [6] Gorecki, A., Brambilla, A., Moulin, V., Gaborieau, E., Radisson, P., and Verger, L., “Comparing performances of a cde x-ray spectroscopic detector and an x-ray dual-energy sandwich detector,” *J. Instrumentation* **8**(11), P11011 (2013).
- [7] Johnson, T. R. C. e. a., “Material differentiation by dual energy ct: initial experience,” *European Radiology* **17**(6), 1510–1517 (2007).
- [8] Engler, P.; Friedman, W. D., “Review of dual-energy computed tomography techniques,” *Materials Evaluation* **48**, 623–629 (1990).
- [9] Yuan, Y., Tracey, B., and Miller, E., “Robust x-ray based material identification using multi-energy sinogram decomposition,” *Proc. SPIE* **9847**, 98470V–98470V–13 (2016).
- [10] Kim, K., Ye, J. C., Worstell, W., Ouyang, J., Rakvongthai, Y., El Fakhri, G., and Li, Q., “Sparse-view spectral ct reconstruction using spectral patch-based low-rank penalty,” *IEEE transactions on medical imaging* **34**(3), 748–760 (2015).
- [11] Han, Y. S., Jin, K. H., Kim, K., and Ye, J. C., “Sparse-view x-ray spectral ct reconstruction using annihilating filter-based low rank hankel matrix approach,” in [*Biomedical Imaging (ISBI), 2016 IEEE 13th International Symposium on*], 573–576, IEEE (2016).
- [12] Yazdanpanah, A. P., Regentova, E. E., and Bebis, G., “Algebraic iterative reconstruction-reprojection (airr) method for high performance sparse-view ct reconstruction,” *Appl. Math* **10**(6), 1–8 (2016).
- [13] Norton, S. J., “Compton scattering tomography,” *Journal of applied physics* **76.4**, 2007–2015 (1994).
- [14] Lange, Axel, e. a., “X-ray compton tomography,” *11th European Conference on Non-Destructive Testing (ECNDT 2014)October 6-10, Prague, Czech Republic* **21.5** (2014).
- [15] Pfeiffer, F., Bech, M., Bunk, O., Kraft, P., Eikenberry, E. F., Brönnimann, C., Grünzweig, C., and David, C., “Hard-x-ray dark-field imaging using a grating interferometer,” *Nature materials* **7**(2), 134–137 (2008).

- [16] W.cong and G.Wang, “X-ray scattering tomography for biological applications,” *Journal of X-Ray Science and Technology* **19**(2), 219–227 (2011).
- [17] Truong, T. T. and Nguyen, M. K., [*Recent Developments on Compton Scatter Tomography: Theory and Numerical Simulations*], INTECH Open Access (2012).
- [18] Kondic, N., Jacobs, A., and Ebert, D., [*Three-dimensional density field determination by external stationary detectors and gamma sources using selective scattering*], Thermal hydraulics of nuclear reactors (1983).
- [19] Zhao, F., Schotland, J. C., and Markel, V. A., “Inversion of the star transform,” *Inverse Problems* **30**(105001), 10 (2014).
- [20] Krylov, R. and Katsevich, A., “Inversion of the broken ray transform in the case of energy-dependent attenuation,” *Physics in Medicine and Biology* **60**(4313), 11 (2015).
- [21] Golosio, B. e. a., “Internal elemental microanalysis combining x-ray fluorescence, compton and transmission tomography,” *Journal of applied Physics* **94**(1), 145–156 (2003).
- [22] Darbon, J., Cunha, A., Chan, T. F., Osher, S., and Jensen, G. J., “Fast nonlocal filtering applied to electron cryomicroscopy,” in [*Biomedical Imaging: From Nano to Macro, 2008. ISBI 2008. 5th IEEE International Symposium on*], 1331–1334, IEEE (2008).
- [23] Semerci, O. and Miller, E. L., “A parametric level-set approach to simultaneous object identification and background reconstruction for dual-energy computed tomography,” *Image Processing, IEEE Transactions on* **21.5**, 2719–2734 (2012).
- [24] Desmal, A. and Bağcı, H., “Sparse electromagnetic imaging using nonlinear landweber iterations,” *Progress In Electromagnetics Research* (2015).
- [25] Desmal, A. and Bağcı, H., “Sparse electromagnetic imaging using nonlinear iterative shrinkage thresholding,” in [*Antennas and Propagation (EuCAP), 2015 9th European Conference on*], 1–4, IEEE (2015).
- [26] Desmal, A. and Bağcı, H., “Three-dimensional sparse electromagnetic imaging accelerated by projected steepest descent,” in [*Antennas and Propagation (APSURSI), 2016 IEEE International Symposium on*], 1029–1030, IEEE (2016).
- [27] Tracey, B. H. and Miller, E. L., “Stabilizing dual-energy x-ray computed tomography reconstructions using patch-based regularization,” *Inverse Problems* **31**(10) (2015).
- [28] Romano, Y., Elad, M., and Milanfar, P., “The little engine that could: Regularization by denoising (red),” *arXiv preprint arXiv:1611.02862* (2016).